Aerosol Science and Technology

ISSN: 0278-6826 (Print) 1521-7388 (Online) Journal homepage: https://www.tandfonline.com/loi/uast20

Predicting the deposition spot radius and the nanoparticle concentration distribution in an electrostatic precipitator

Calle Preger, Niels C. Overgaard, Maria E. Messing & Martin H. Magnusson

To cite this article: Calle Preger, Niels C. Overgaard, Maria E. Messing & Martin H. Magnusson (2020) Predicting the deposition spot radius and the nanoparticle concentration distribution in an electrostatic precipitator, Aerosol Science and Technology, 54:6, 718-728, DOI: 10.1080/02786826.2020.1716939

To link to this article: https://doi.org/10.1080/02786826.2020.1716939

AEROSOL SCIENCE AND TECHNOLOGY
2020, VOL. 54, NO. 6, 718–728
https://doi.org/10.1080/02786826.2020.1716939

Predicting the deposition spot radius and the nanoparticle concentration distribution in an electrostatic precipitator

Calle Preger[a], Niels C. Overgaard[b], Maria E. Messing[a], and Martin H. Magnusson[a]

[a]NanoLund and Solid State Physics, Lund University, Lund, Sweden; [b]Centre for Mathematical Sciences, Lund University, Lund, Sweden

ABSTRACT

Deposition of aerosol nanoparticles using an electrostatic precipitator is widely used in the aerosol community. Despite this, basic knowledge regarding what governs the deposition has been missing. This concerns the prediction of the size of the particle collection zone, but also, perhaps more importantly, prediction of the nanoparticle concentration distribution on the substrate, both of which are necessary to achieve faster and more precise deposition. In this article, we have used COMSOL Multiphysics simulations, experimental depositions, and two analytical models to describe the deposition. Based on that, we propose a simple equation that can be used to predict the size of the deposition spot as well as the particle concentration on the substrate. The equation we derive concludes that the size of the deposition spot only depends on the gas flow rate into the precipitator, and on the constant drift velocity of a particle in an electric field. The equation also displays that the deposited particle concentration is independent of the gas flow rate. Our general mathematical analysis has great applicability, as it can be used to model different geometries and different types of deposition methods than the one described in this article. We can therefore also propose that the drift velocity in this model easily could be replaced by another velocity acting on the particles at other deposition conditions, for instance, the thermophoretic velocity during thermophoretic deposition. This would result in the same dependence as presented in this article. Finally, we demonstrate analytically and through experiment that the particle distribution inside the spot will be homogenous and follows a top hat profile.

ARTICLE HISTORY
Received 16 October 2019
Accepted 8 January 2020

EDITOR
Mark Swihart

Introduction

In order to perform detailed characterization of engineered aerosol nanoparticles, or to investigate the ultra-fine particles that surround us in the atmosphere, it is preferable to first collect such particles onto a substrate for *ex situ* characterization. Even though *in situ* and in-flight characterization techniques of aerosols have improved greatly in the last years (McKibbin et al. 2019; Ouf et al. 2016), *ex situ* characterization, using electron microscopy or x-ray methods on already collected particles are still the standard way to characterize aerosol nanoparticles. The deposition and collection of aerosol nanoparticles can be achieved in several different ways. Due to their low inertia, it is usually necessary to expose these particles to an external force, such as thermophoretic, or electric, in order to capture them. Thermophoretic deposition has the advantage of not being charge dependent, but has the disadvantage of it being challenging to achieve a homogeneous field and deposition. On the other hand, deposition using electric forces, using a so-called electrostatic precipitator (ESP), has the advantage of being simple and straightforward. An electric potential is applied to a surface, and the particles are collected on that surface. However, for this to work, the particles must carry a charge upon deposition, but this can be achieved, if the particles are not already charged, by simply adding a particle charger before deposition. ESPs can, for instance, be used in portable samplers (Fierz, Kaegi, and Burtscher 2007) or incorporated into closed systems for collection of generated engineered

CONTACT Calle Preger calle.preger@ftf.lth.se Solid State Physics and NanoLund, Lund University, Box 118, Lund 221 00, Sweden.
Supplemental data for this article is available online at https://doi.org/10.1080/02786826.2020.1716939.
Color versions of one or more of the figures in the article can be found online at www.tandfonline.com/uast.

nanoparticles (Messing et al. 2009). ESPs can also be used as filters, in order to clean a gas from harmful particles (Pavlish et al. 2003).

There are several different types of ESPs. Traditionally, the parallel plate (Liu, Whitby, and Yu 1967), and the point-to-plate setup (Cheng, Yeh, and Kanapilly 1981) have been used frequently, however both these have the drawback of low particle collection efficiency. Twenty years ago, in this journal, Dixkens and Fissan (1999), described a new concept for an ESP, where charged nanoparticles could be deposited with 100% sampling efficiency. In their proposed setup, the aerosol flows vertically downward until it reaches a plate exposed to a high constant electrical potential. The gas flow expands radially and the particles that carry the opposite charge with respect to the plate are deposited. In their publication, they were able to demonstrate experimentally that the charged particles were collected in a circular zone, or a spot, and that the particle concentration in this collection spot was approximately uniform. They were also able to show that the size of this spot depended on the gas flow rate and the electrical mobility of the particles. This has been shown again experimentally, when the spot radius of an ESP was studied when alternating the particle diameter and applied potential (Kala et al. 2012). It was also shown experimentally by Fierz, Kaegi, and Burtscher (2007), where the sampling efficiency was affected by electrical mobility of the particles and that smaller particles were focused more toward the center. Nevertheless, the exact relation between the size of this deposition spot and the deposition parameters has, until now, been unknown and was generally assumed to depend on the design of the individual ESP, requiring calibration.

Few studies have aimed to describe the macroscopic aspects of the particle deposition in an ESP. Instead, plenty of research have been dedicated to understanding the microscopic aspects of the deposition in an electric field, studying the particle–particle interaction and particle–substrate interaction close to the substrate (You and Choi 2007; Krinke et al. 2002; Zhuang et al. 2000). These studies have used numerical simulations in combination with experimental validation to study and control the deposition, and from this being able to refine the deposition to make elegant nanostructures with high precision (Kim et al. 2006; Choi et al. 2015; You and Choi 2007; Krinke et al. 2001). Although these studies have been essential for generation of fine nanostructures, studying the macroscopic aspects is still crucial for optimization of the aerosol nanoparticle deposition by, for instance, determining what governs the particle deposition distribution and the collection zone.

In this study, we have used experiments, numerical simulation, and mathematical models to study the macroscopic aspects of aerosol deposition in an ESP similar to the one described by Dixkens and Fissan (1999). From this, we were able to determine the particle distribution, concentration, as well as the exact relation between the deposition parameters and the size of the deposition spot size. COMSOL Multiphysics has been used to perform numerical experiments, by using a model of the ESP similar to that used in our lab. From these results, we observed a homogenous particle concentration within the spot, when depositing monodisperse singly charged nanoparticles, and obtained a semi-empirical equation that describes the relation between the deposition spot size and the deposition parameters. This equation shows great agreement with experimental results from real depositions, when measuring the deposited particle concentration by scanning electron microscopy (SEM). Furthermore, this semi-empirical equation, as well as the particle distribution, has been confirmed by analytical analysis in a simplified geometry, in excellent agreement with the experimental results. Lastly, we describe the deposition in more general terms, showing that the same equation can be used for different geometries and situations.

The proposed equation is remarkably simple and will be valuable when performing deposition of nanoparticles. This equation can be used to predict the nanoparticle concentration on the substrate. This is of large importance when studying the magnetic or catalytic properties of engineered nanoparticles, or when forming semiconducting nanostructures (Preger et al. 2019; Messing et al. 2010; Magnusson et al. 2014). Also, by varying the applied electrical potential, it is possible to tune the spot size to match the desired substrate, in order to minimize the deposition time and avoid waste of particles. By understanding the basic variables that will affect the deposition, new better designs can be made to increase the collection efficiency. Finally, this study also demonstrates the possibilities to use COMSOL Multiphysics to simulate the macroscopic trajectories of a collection of aerosol nanoparticles, with results that agree with the real experiment. This knowledge will be practical when designing new aerosol systems or evaluating existing ones.

Method

Comsol simulations

A 2D replica of the ESP chamber used in our lab was constructed within the COMSOL Multiphysics 5.3

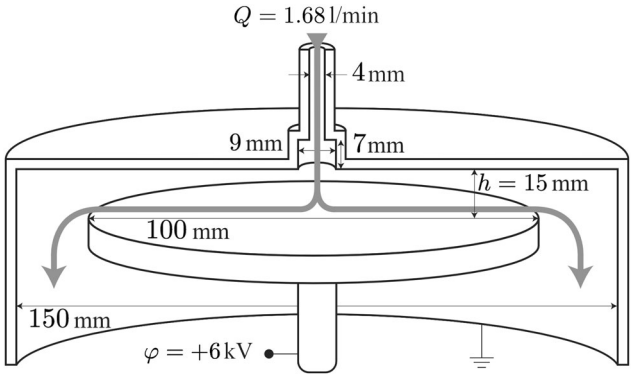

Figure 1. Schematic of the ESP used for the experimental results and as the model for the COMSOL simulations. The aerosol enters the ESP with the gas and flows vertically downwards toward the deposition plate. The deposition plate has an applied electrical potential, which creates an electric field strong enough to deposit the particles.

software, and a schematic of such an ESP can be seen in Figure 1. The simulations were performed in two steps: first the surrounding physics was determined, i.e., the gas flow profile and the electric field, and then the particle trajectories were simulated. During the second simulation step, between 500 and 1000 monodisperse, singly negatively charged particles, with identical electrical mobility, were released. Their trajectories were solved within the software, by using Newton's second law to calculate the change in particle momentum,

$$m_\mathrm{p}\frac{d\boldsymbol{v}_\mathbf{p}}{dt} = F_\mathrm{D} + F_\mathrm{E} + F_\mathrm{B} + (F_\mathrm{M} + F_\mathrm{th}) \qquad (1)$$

where F_D is the drag force, F_E is the electrostatic force, and F_B is the Brownian force. If necessary, Equation (1) can be extended with other forces, e.g., magnetic F_M or thermophoretic F_th. However, in this case, we decided to only evaluate the first three mentioned forces.

Brownian displacement during flight and particle–particle interaction close to the surface will naturally affect the final position of a single particle (Krinke et al. 2002). Despite this, we argue that they can both be ignored in this study. The particles are, typically, inside the ESP less than 1 s before reaching the plate, and the Brownian displacement for nanoparticles during 1 s is in the order of 0.01–0.1 mm (Hinds 1999). This displacement is much smaller than the radius of the deposition spot, which ranges from a few mm to tens of mm. Since we are looking at the collective behavior of a large number of particles and not the exact position of a single particle, this displacement can, potentially, be ignored. The ineffectiveness of Brownian displacement on the macroscopic deposition was verified by comparing simulations with and without Brownian force, see Figure S1 in the online supplementary information (SI). Crucially, by including Brownian force in the simulation, the computational time became more than 200 times longer, and since the effect on the deposition spot was minor, the Brownian force was neglected in the following simulations. The particle–particle interactions were also regarded as negligible: the concentration of particles in the gas flow during real experiments was $< 10^6\,\mathrm{cm}^{-3}$, meaning that the particle–particle distance is on average $> 100\,\mu\mathrm{m}$ and this will not affect the particles. The electrostatic force and the drag force are thus the dominant forces that will govern the size of the deposition spot.

Experimental depositions

The nanoparticles were generated by spark ablation (Schwyn, Garwin, and Schmidt-Ott 1988; Pfeiffer, Feng, and Schmidt-Ott 2014; Meuller et al. 2012) by using pure metal electrodes as the seed material in a nitrogen gas flow (99.9999%) controlled by mass flow controllers. After the spark, the formed agglomerates are charged in a bipolar diffusion charger (Wiedensohler 1988), then size selected with a first differential mobility analyzer (DMA) (TSI 3081 Long). Next, the agglomerates are reshaped to compacted particles when heated above the compaction temperature (Karlsson et al. 2005; Hallberg et al. 2017) in a tube furnace (Lenton LTF). The compacted particles are size selected again with a second DMA (a custom built Vienna type (Knutson and Whitby 1975)) before being deposited onto a Si substrate. All the deposited particles will therefore have the same electrical mobility and the particle concentration is continuously measured with an electrometer (TSI 3086B). In between depositions, the deposition chamber is isolated from the aerosol flow, and during deposition, the electric field is applied a few seconds after the pressure in the system has been stabilized after letting the gas pass through. All depositions were at least 5 min long to ensure that small variations in the beginning of the deposition would not have an impact on the deposited particle concentration. To analyze the depositions, multiple images were acquired using a SEM (Hitachi SU8010), and the particle concentration on the substrates was determined using ImageJ (Schneider, Rasband, and Eliceiri 2012). Example images showing a selection of the deposited particles can be found in SI Figure S2.

Results

COMSOL simulations and experimental results

Dixkens and Fissan (1999) reported that the concentration profile of the deposited nanoparticles follows a

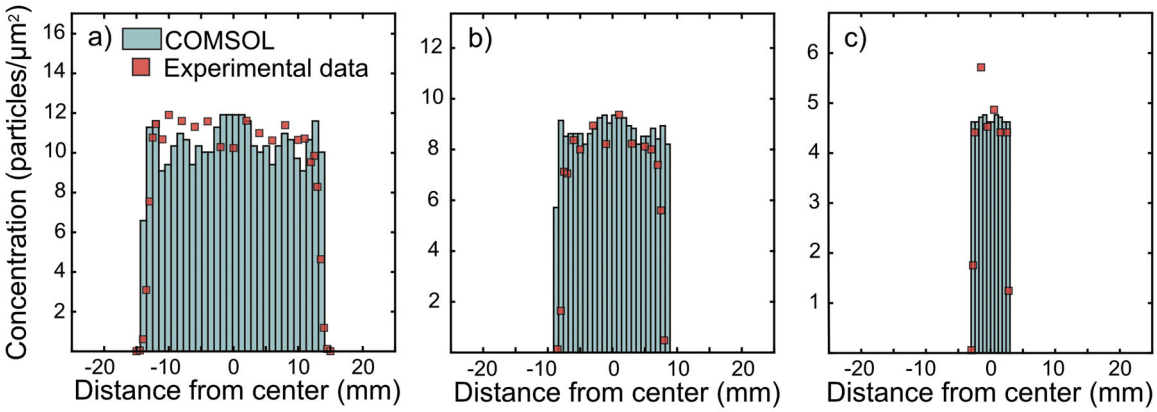

Figure 2. Simulated and experimentally measured surface particle concentration, plotted against the distance from the center point for three different particle sizes (a) 50 nm, (b) 30 nm, and (c) 10 nm. In all cases, the applied electric field was 6 kV, the gas flow rate 1.68 slm ($2.8{\cdot}10^{-5}$ m^3 s^{-1}) and distance between the inlet and deposition plate 13.4 mm. The radius of the deposition spot is given by half the width of the top hat profile. All three sizes showed good agreement between the experiments and the simulations. The heights of the histograms have been rescaled to match the experimental data points.

so called top hat profile, with constant concentration within the deposition spot and a sharp, distinct concentration drop to zero at the edge. They also demonstrated that the shape of this spot is close to a perfect circle. The COMSOL simulations in this work were performed using a 2D model of the ESP, hence the concentration profile is measured along a line, and not a circle. For each simulation, 500 particles were released and deposited. The concentration profiles obtained from the COMSOL simulations displayed the same characteristic top hat profile as has been reported earlier, with constant concentration in the center, and with sharp, distinct edges where the concentration of particles drops down to zero, see histogram in Figure 2. These profiles were compared to experimental concentration profiles using the same deposition parameters (6 kV as the applied electric potential, 1.68 slm ($2.8{\cdot}10^{-5}$ m^3 s^{-1}) as the gas flow rate, and 13.4 mm as the distance between the inlet and deposition plate) for three different particle diameters (50, 30 and 10 nm), see red squares in Figure 2. As demonstrated in Figure 2, the experimental results are in good agreement with simulations regardless of nanoparticle size, and the characteristic top hat profiles with distinct edges can be observed in all three cases. From the experimental data points we can observe small tails at the edges, which might be due to the size distribution not being completely monodisperse when size selecting with a DMA.

To determine the exact relation between the size of the spot radius and the different deposition variables, simulations to investigate each variable were performed. From this, it was concluded that only four variables had a considerable impact on the spot radius; the gas flow rate (Q), the distance between the inlet and the deposition plate (h), the applied electrical potential to the plate (φ), and the electrical mobility of the nanoparticles (Z). Each of these four variables was systematically studied to obtain their exact relation to the spot radius (r_{spot}), see Figure 3. For each studied variable, all other variables were kept fixed, and the results were fitted to find the specific relation, tabulated values can be found in Table S1. All four variables had an almost perfect square root or inverse square root dependence, and were combined into the following semi-empirical equation,

$$r_{spot} = \kappa\sqrt{\frac{Qh}{\varphi Z}} \tag{2}$$

where the constant κ in Equation (2) is dimensionless when the other variables are given in SI units.

Apart from the above-mentioned variables, several other parameters were investigated using COMSOL Multiphysics. The gas velocity at the inlet did not have a large impact on the spot radius; this was studied by keeping the gas flow fixed and changing the radius of the inlet. A deviation from Equation (2) was observed only for extremely large and small inlet radii. When the inlet diameter became much larger than the distance to the plate, the spot radius increased slightly. Whether this was due to the low gas velocity or disturbance in the electric field is not certain. For small inlet radii, when the gas velocity became much larger than the 2 m s^{-1} used in the experimental results, impaction started to influence the deposition significantly. Although the spot radius was almost unaffected, the particle concentration profile changed with an increased concentration in the center region, especially for the larger particles. The

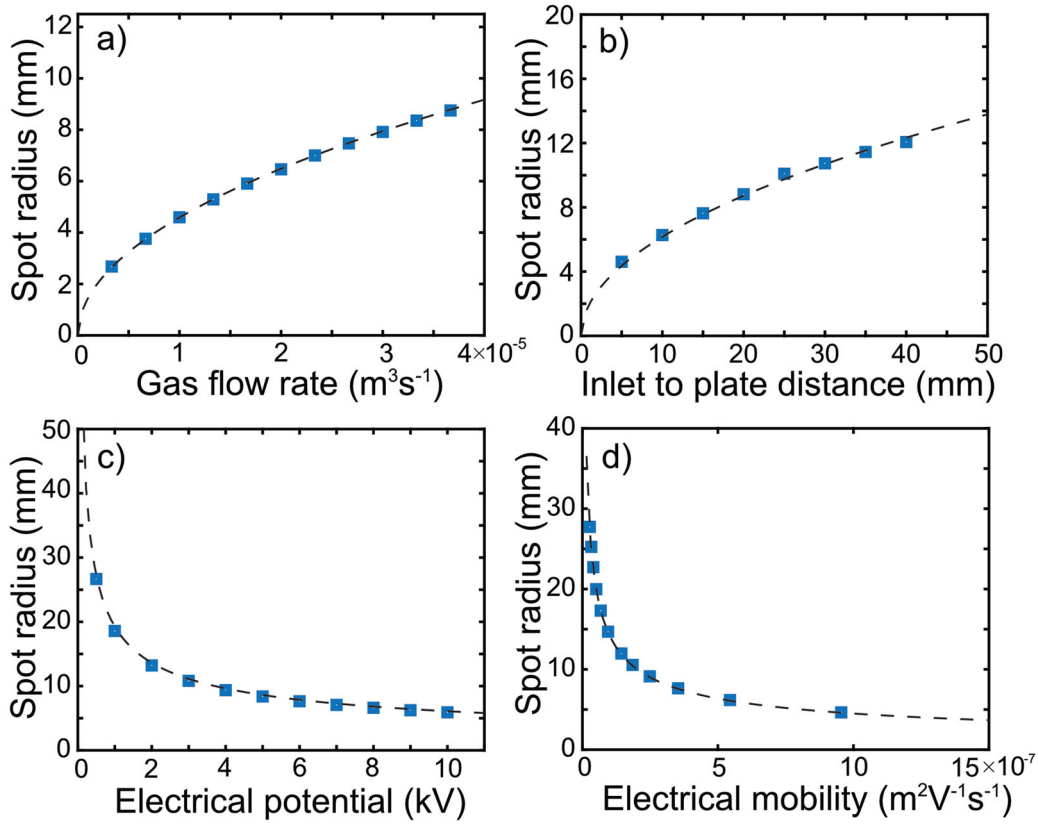

Figure 3. Data points extracted from the COMSOL simulations. The spot radius plotted against (a) the gas flow rate, (b) the distance between the inlet and the plate, (c) the applied electrical potential, and (d) the electrical mobility of the particles. For each variable, the other variables were kept constant. Each graph is plotted together with a fitted square root or inverse square root dependence (black dashed line).

effect of impaction is therefore important to be aware of and should be studied further since it will affect the deposition profile when the gas flow is high or inlet radius small. However, in this article, we study the system when it is the regime where impaction is negligible. The composition of the particles, i.e., the mass density, had no effect on the spot radius or the concentration profile when varying the density from 1000 kg m^{-3} to 19 300 kg m^{-3}. Furthermore, variations in the diameter of the cylindrical housing and of the collection plate, the location of the gas outlet, and the width of the inlet nozzle were all also investigated. A minor deviation from Equation (2) was in those cases observed only when the collection plate was of a similar size as the deposition spot. Although the specific geometry had no effect on the deposition spot, the size of ESP in the following simulations was, for simplicity, based on the actual one used during experiments.

To validate Equation (2), as well as the simulated data points, experimental depositions were performed with different values of the deposition variables to obtain a variety of differently sized deposition spots, with radii ranging from 3 mm to 25 mm. The depositions were performed using size selected Cu or Bi nanoparticles of different sizes (15–45 nm), applied electrical potentials (2000–8000 V), distances between inlet and plate (13.4–30.2 mm), and gas flow Q constantly set to 1.68 slm ($2.8{\cdot}10^{-5}$ m^3 s^{-1}). The spot radius was calculated using the following relation,

$$\pi r_{\text{spot}}^2 = \frac{Qtc_{\text{gas}}}{c_{\text{spot}}} \tag{3}$$

where the total number of deposited particles is divided by the particle concentration in the spot c_{spot}, assuming no particle losses and the spot being shaped as a perfect circle. The assumption of homogenous concentration inside the spot is based on the results presented in Figure 2, and the approximation of a perfect circle is motivated by the results presented by Dixkens and Fissan (1999) as well as from our own observations. Details describing each deposition can be found tabulated in SI Table S2. These calculated experimental spot radii are plotted against Equation (2), see red squares in Figure 4, together with the simulated data points (blue crosses) showing excellent agreement. The data points follow a straight line

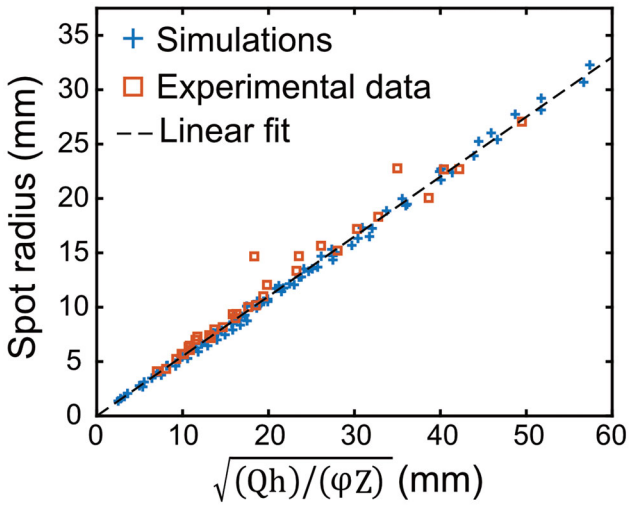

Figure 4. Simulated data points (blue crosses) plotted together with the experimentally determined spot radii (red squares) against Equation (2). From the linear fit (black dashed line) the dimensionless constant κ was determined to 0.55.

(black dashed line) and from this, the dimensionless constant κ in Equation (2) was determined to 0.55.

A first analytical model

To understand Equation (2) analytically, it is much easier if we first rewrite it. The ratio h/φ can be replaced with $1/E$, where E is the electric field, approximated as infinite parallel plates. Since $EZ = v_d$, which is the constant drift velocity of a charged particle in the presence of an electric field, Equation (2) can be rewritten as,

$$r_{spot} = \kappa\sqrt{\frac{Q}{v_d}}. \tag{4}$$

The spot radius will therefore depend only on the gas flow and the particle drift velocity. Let us now consider a simplified gas geometry. Due to the axial symmetry of the ESP, it is natural to describe the system in cylindrical coordinates. We let the z-axis originate from the deposition plate and point up toward the center of the circular inlet. The r-axis will then simply follow along the deposition plate, see Figure 5. In analogy with the real ESP, we let the gas initially flow in negative z-direction, perpendicular to the plate, but as it reaches the obstacle, the deposition plate, it turns and expands along the r-direction, as a cylinder with constant height. This behavior is similar to what we have observed in the COMSOL simulations, see colored profile in Figure 5a. The growth of this disc-like gas flow will result in a radial gas velocity that is proportional to $1/r$. We further assume that the gas flowing parallel to the substrate behaves as if it would flow between two parallel plates with some flow profile $f(z)$, drawn as roughly parabolic function in Figure 5b. The flow profile $f(z)$ is an arbitrary, positive, continuous function for $0 < z < h$, with the no-slip boundary conditions, $f(0) = 0$ and $f(h) = 0$. The mass conservation for the gas then implies the condition,

$$Q = 2\pi r \int_0^h f(z)/r \; dz, \tag{5}$$

which states that the gas flow rate Q in the ESP must be equal to the flow of the velocity field through any cylindrical surface inside the precipitator. If we also assume that the incoming gas flow is narrow compared to the spot size, then the radial flow can be modeled as a line source along the z-axis. The charged nanoparticles will travel with this gas flow in the r-direction with the velocity $v_r = f(z)/r$, and due to the electric field, with a perpendicular drift velocity, $v_z = -v_d = -ZE$.

We want to determine the trajectory of a nanoparticle that enters the convective flow at the point $(r_0,\ z_0)$ at time $t = 0$. If we denote this trajectory $(r(t),\ z(t))$ and use the description for the velocities, then we can rewrite it as a system of first order differential equations,

$$\begin{cases} r'(t) = f(z(t))\dfrac{1}{r(t)} \\ z'(t) = -v_d \end{cases} \tag{6}$$

with the initial condition $(r(0), z(0)) = (r_0, z_0)$. The solution to this initial value problem is then seen to be

$$\begin{cases} z(t) = z_0 - v_d t \\ v_d\pi r(t)^2 - \ v_d\pi r_0^2 = q(z_0) - \ q(z(t)) \end{cases} \tag{7}$$

where $q(z) = 2\pi\int_0^z f(s)ds$ is the primitive function of $2\pi f(z)$. The function $q(z)$ can be interpreted as the partial gas flow, and equals the amount of gas injected into to ESP per unit time of a line source lying between 0 and z. Since $q(0) = 0$, it follows from Equation (5) that, $q(h) = Q$. From Equation (7), the particle trajectories can be described as the curves in the (r, z)-plane which satisfy equations of the form

$$v_d\pi r^2 + \ q(z) = C, \tag{8}$$

where C is a nonnegative constant which may be determined from the initial conditions. Different constants correspond to different particle trajectories, and since the ESP operates in steady state, time can be eliminated from our description.

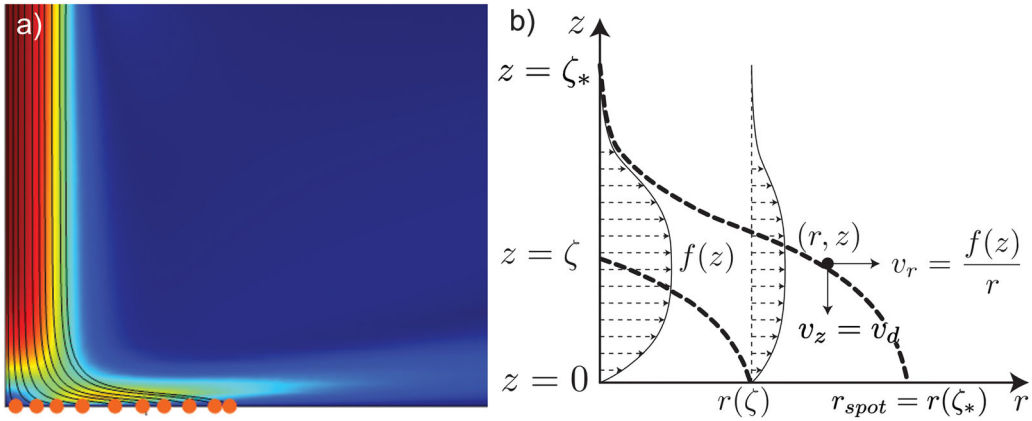

Figure 5. (a) COMSOL simulations of the gas speed (colored) and the particle trajectories (black lines and orange spheres) indicating our model predictions. (b) The particle will, in this model, have a velocity in both the *r*- and *z*-direction. The velocity in the *z*-direction is governed by the constant drift velocity (v_d) and the velocity in the *r*-direction is governed by the gas flow. The gas flow profile *f(z)* will have both a *z*- and an *r*-dependence, where the velocity is proportional to 1/*r*.

Next, we let $(r_0, z_0) = (0, \zeta)$, where $0 \leq \zeta \leq h$ is a point on the z-axis inside the ESP. As long as $f(\zeta)$ is positive, a particle trajectory will emanate from this point, and according to Equations (7) and (8), this trajectory will then consist of the points (r, z) which satisfy the equation

$$v_d \pi r^2 + q(z) = q(\zeta). \tag{9}$$

This trajectory will intersect the deposition plate at some point $(r, z) = (r(\zeta), 0)$, and from Equation (9), we get the following, important, relation between the z-coordinate ζ of the injection point and the distance $r(\zeta)$ from the deposition point to the z-axis,

$$v_d \pi r(\zeta)^2 = q(\zeta) \tag{10}$$

The function q is monotonically increasing, and therefore the function $r(\zeta)$ also has to increase monotonically with ζ as long as $f(\zeta) > 0$, which is the condition for a trajectory emanating from the point $(0, \zeta)$. The maximum value of $r(\zeta)$ will therefore be the same as the deposition spot radius, r_{spot}. If we let ζ_* denote the smallest number, such that $f(z) = 0$ for all $z > \zeta_*$, then $r_{\text{spot}} = r(\zeta_*)$. Since we also have $q(\zeta_*) = q(h) = Q$, then it follows from Equation (10) that $v_d \pi r_{\text{spot}}^2 = Q$. In other words, we get an analytical expression for the radius of the deposition spot:

$$r_{\text{spot}} = \sqrt{\frac{Q}{\pi v_d}}, \tag{11}$$

which would make the factor κ in Equation (4) be $\sqrt{1/\pi} = 0.56$, in excellent agreement with both experiment and simulation. Also, by combining Equation (3) and Equation (11),

$$c_{\text{spot}} = c_{\text{gas}} v_d t \tag{12}$$

we notice that the deposited particle concentration inside the spot is independent of the gas flow rate. This implies that perfect control of the gas flow rate will not be necessary to predict the deposited particle concentration on the substrate. Knowing the exact gas flow rate will only be necessary when predicting the size of the deposition spot. This shows, in theory, that it would be possible to split the gas into multiple parts and run several ESPs in parallel and still obtain the same concentration on each substrate as one would by running a single ESP.

Lastly, we can use the relation in Equation (10) to demonstrate the top hat property of the deposition. We let $N(r)$ denote the number of particles deposited per unit time onto an arbitrary disc on the deposition plate with the radius r and the origin at its center. If r is less than r_{spot}, then the point $(r, 0)$ is reached by a particle trajectory emanating at some point $(0, \zeta)$ on the z-axis, thus $r = r(\zeta)$ is a function of ζ. Since every point on the disc is reached by a particle trajectory emanating from some point on the segment $0 < z < \zeta$ on the z-axis, it follows that

$$N(r(\zeta)) = c_{\text{gas}} q(\zeta), \tag{13}$$

where $q(\zeta)$ is the rate of flow of the gas from the part of the line source which lies below the level ζ. If r is larger than r_{spot} then no further trajectory reaches the disc and one simply has $N(r) = N(r_{\text{spot}})$. By combining this with the relation found in Equation (10), then the following expression for N emerges

$$N(r) = \begin{cases} c_{\text{gas}} u_d \pi r^2 & \text{for } r \le r_{spot}, \\ c_{\text{gas}} u_d \pi r_{\text{spot}}^2 & \text{for } r \ge r_{spot}. \end{cases} \tag{14}$$

This shows that $N(r)$ is directly proportional to the area of the disc whenever the radius r is less than r_{spot}, which proves that the particle concentration inside the deposition spot is homogeneous. It also shows that $N(r)$ is constant if r is greater than r_{spot}, hence the particle concentration outside the spot is zero, which describes the desired top hat profile.

A second, complementary, and more general model

In this final section, we perform a second, slightly more advanced, derivation of the equation describing the spot radius and the top hat distribution. This approach is based on an analysis of the partial differential equation (PDE) governing the concentration of the nanoparticles inside the ESP, instead of the velocities as in the previous section. This new model is more general than the first one and has greater applicability. In particular, it avoids the specific simplifying assumption on the gas flow, which played such a central part in the explicit calculations of the first model.

As mentioned in the earlier sections, the ESP operates at steady state, hence the concentration of the particles will be independent of time. Instead, it will be a function of the position $\boldsymbol{x}$ inside the ESP: $u = u(\boldsymbol{x})$. The same holds for the convective field $\boldsymbol{w} = \boldsymbol{w}(\boldsymbol{x})$, which is the sum of the steady velocity field $\boldsymbol{v} = \boldsymbol{v}(\boldsymbol{x})$ of the gas flow and the drift induced by the electrostatic field $Z\boldsymbol{E}(\boldsymbol{x})$. If diffusion effects are ignored, as they have been throughout this article, the nanoparticle concentration will be governed by the transport PDE,

$$\frac{\partial u}{\partial t} = -\nabla \cdot (u\boldsymbol{w}), \tag{15}$$

where $\partial u/\partial t = 0$ at steady state. In fact, the vector $\boldsymbol{J} = u\boldsymbol{w}$ corresponds to the flux of particles in the ESP, so the above PDE follows by application of the equation of continuity (or conservation law) $\partial u/\partial t = -\nabla \cdot \boldsymbol{J}$ to this flux, see, e.g., Logan (1994). The particle concentration on the top plate of the ESP is denoted u_0, and this concentration is assumed to be known in advance. Our task will be to solve the PDE and compute the flux $\boldsymbol{J} = u\boldsymbol{w}$ of the nanoparticles on the bottom plate, since the normal component of this vector corresponds to the deposition rate of particles there.

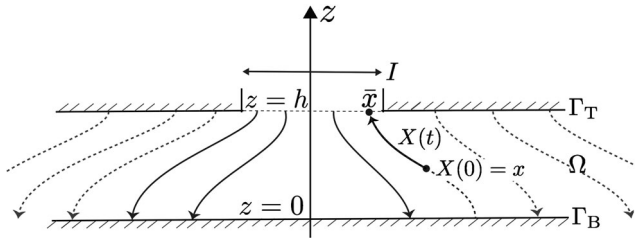

Figure 6. Illustration of the region Ω, corresponding to the inside of the ESP. From each point on the boundary Γ_B, there exists a trajectory emanating from the boundary Γ_T. We solve this by following such trajectory ***X(t)*** upstream until it reaches Γ_T. If this trajectory originates from the region *I*, the particle concentration along this trajectory will be c_{gas}; else it will be zero.

The inside of the ESP is modeled as the open set Ω, consisting of the points between two parallel, infinite, planes separated by a distance h

$$\Omega = \{\boldsymbol{x} = (x, y, z) \in R^3 : \ 0 < z < h\}, \tag{16}$$

see Figure 6. The boundary of Ω consists of two disjoint parts, the bottom deposition plate $\Gamma_B = \{\boldsymbol{x} : \ z = 0\}$ and the top inlet plate $\Gamma_T = \{\boldsymbol{x} : \ z = h\}$. The aerosol inlet itself is a part I of the top plate which is bounded and open when considered as a subset of Γ_T. Our model requires us to solve the following so-called Cauchy problem for the steady state transport PDE:

$$\begin{cases} -\nabla \cdot (u\boldsymbol{w}) = 0 \ \textit{in} \ \Omega \\ u = u_0 \ \textit{on} \ \Gamma_T. \end{cases} \tag{17}$$

The deposition rate on the bottom plate will then be given by $u\boldsymbol{w} \cdot \mathbf{n}(\boldsymbol{x})$ on Γ_B where $\mathbf{n}(\boldsymbol{x})$ is the outward unit normal to Ω at $\boldsymbol{x} \in \Gamma_B$, which equals $(0, 0, -1)$ in our simplified geometry. The equations in (17) can be simplified by adding the fact that the convective field $\boldsymbol{w}$ in the ESP is approximately divergence free. In fact, the velocity field $\boldsymbol{v}$ of the gas is practically divergence free for flow speeds well below the speed of sound. Also, at particle concentrations and electric field strengths relevant for many aerosol applications, the particle–particle force will be about 10^6 times weaker than the force exerted by the field. Therefore, $\nabla \cdot \boldsymbol{E} = \rho/\varepsilon_0 \approx 0$, and in summary, we let $\nabla \cdot \boldsymbol{w} = 0$ and rewrite Equation (17) to the following,

$$\begin{cases} \boldsymbol{w} \cdot \nabla u = 0 \ \textit{in} \ \Omega \\ u = u_0 \ \textit{on} \ \Gamma_T. \end{cases} \tag{18}$$

We solve this Cauchy problem by the method of characteristics, see John (1982). This consists in following the flow line of a particle upstream, in reverse time, from a point $\boldsymbol{x}$ inside the ESP, until it reaches the top

plate at some point $\bar{\boldsymbol{x}}$, see Figure 6. The concentration $u_0(\bar{\boldsymbol{x}})$, which is prescribed in advance, is then used to infer $u(\boldsymbol{x})$ itself, as we shall see below, and the PDE is solved.

In order to carry out this analysis analytically, we let $\boldsymbol{x} \in \Omega$ be an arbitrary point inside the ESP and let the particle trajectory, denoted as $\boldsymbol{X} = \boldsymbol{X}(t)$, pass through this point at time $t = 0$. The curve $\boldsymbol{X}(t)$ is called the characteristic of the PDE in Equation (18) and is the solution of the following system of ordinary differential equations,

$$\begin{cases} \dot{\boldsymbol{X}}(t) = -\boldsymbol{w}(\boldsymbol{X}(t)) \\ \boldsymbol{X}(0) = \boldsymbol{x}. \end{cases} \tag{19}$$

Suppose $u = u(\boldsymbol{x})$ is a solution to the transport PDE in Equation (18). Then the particle concentration will be constant along any characteristic curves. In fact, if we compute the derivative of u along such a trajectory $\boldsymbol{X}(t)$ we get,

$$\begin{aligned} \frac{d}{dt} u(\boldsymbol{X}(t)) &= -\nabla u(\boldsymbol{X}(t)) \cdot \dot{\boldsymbol{X}}(t) \\ &= -\nabla u(\boldsymbol{X}(t)) \cdot \boldsymbol{w}(\boldsymbol{X}(t)) \\ &= 0 \end{aligned} \tag{20}$$

which by Equation (19), proves the claim. It follows that the concentration $u(\boldsymbol{x})$ equals u_0 at the point where the characteristic curves through $\boldsymbol{x}$ intersects the top plate.

Assuming that the vertical component of $\boldsymbol{w}$ is everywhere bounded away from zero and that the magnitude of $\boldsymbol{w}$ is everywhere bounded above, it can be shown that there exists a finite positive time $t = t(\boldsymbol{x})$ such that the trajectory through $\boldsymbol{x}$ reaches the top plate at this time, that is $\boldsymbol{X}(t(\boldsymbol{x})) \in \Gamma_T$. We let a mapping $\Phi : \Omega \to \Gamma_T$ be defined by setting, $\Phi(\boldsymbol{x}) = \boldsymbol{X}(t(\boldsymbol{x}))$, where $\boldsymbol{X}(t)$ is the solution of Equation (19) for $\boldsymbol{x} \in \Omega$. The domain of definition for Φ can be extended, in a natural way, to include points on the top- and bottom plate, in particular $\Phi(\boldsymbol{x}) = \boldsymbol{x}$ for all points $\boldsymbol{x} \in \Gamma_T$. In view of Equation (20) the solution to the Cauchy problem in Equation (18) can now be written down as

$$u(\boldsymbol{x}) = u_0(\Phi(\boldsymbol{x})) \tag{21}$$

Having obtained the solution of the Cauchy problem in Equation (18) in Equation (21), it is now possible to draw conclusions about the particle deposition on the bottom plate. Notice that, in our practical application, the boundary concentration on the top plate is given by the piecewise constant function

$$u_0(\boldsymbol{x}) = \begin{cases} c_{\text{gas}} \quad \textit{for } \boldsymbol{x} \in I \subset \Gamma_T \\ 0 \ \textit{otherwise}, \end{cases} \tag{22}$$

where the c_{gas} is the constant particle concentration at inlet I. It follows from Equation (21) and Equation (22) that, for $\boldsymbol{x} \in \Gamma_B$, the concentration $u(\boldsymbol{x})$ is either zero or constant c_{gas}, depending on whether Φ maps $\boldsymbol{x}$ to the inlet I or its complement. The particle concentration on the bottom plate is, therefore, found to be piecewise constant.

As mentioned earlier, the deposition rate at some point on the bottom plate equals the normal component of the flux of particles at that point, i.e., equals to $u(\boldsymbol{x})\boldsymbol{w}(\boldsymbol{x}) \cdot \mathbf{n}(\boldsymbol{x}) \in \Gamma_B$. Since the velocity field of the gas flow is zero at the bottom plate (the no-slip condition) the only contribution to $\boldsymbol{w}$ in this point is the electrostatic drift $Z\boldsymbol{E}(\boldsymbol{x})$, which is already normal to the bottom plate. It then follows, that the deposition flux rate is given by,

$$\boldsymbol{J}_{dep} = u(\boldsymbol{x})ZE(\boldsymbol{x}) \text{ for } \boldsymbol{x} \in \Gamma_B \tag{23}$$

where $E(\boldsymbol{x})$ denotes the magnitude of the electric field $\boldsymbol{E}(\boldsymbol{x})$. If, as in the application considered here, the electric field is practically homogeneous, $E(\boldsymbol{x}) = E$ at the bottom plate, then we reach the conclusion that the deposition rate at a certain point is either zero or equal to $c_{\text{gas}}ZE$. Furthermore, if the inlet I is assumed to be circular with its center on the z-axis, and the gas flow is axially symmetric about this axis, then the deposition spot will be a circle, with an area A_{spot}. At steady state, the rate at which the particles enter the ESP at the inlet must be equal to the rate at which the particles are being deposited on the bottom plate. This particle rate at the inlet is simply given by $c_{\text{gas}}Q$ and the deposition rate is the pointwise deposition rate times the entire deposition area, $c_{\text{gas}}ZEA_{\text{spot}}$. Since these two are equal we now find the relation,

$$Q = ZEA_{\text{spot}}. \tag{24}$$

When A_{spot} is a perfect circle, as it is in the axially symmetric case, then the above formula implies,

$$r_{spot} = \sqrt{\frac{Q}{\pi ZE}}, \tag{25}$$

which agrees perfectly with the formula from the previous sections, if we recall that $ZE = v_d$. Thus, our model predicts, again, a top hat distribution for the monodisperse, singly charged particle concentration inside a circular spot with a radius $\sqrt{Q/\pi ZE}$, in excellent agreement with the experiments, simulations, as well as with the simplified analytic model. This model also predicts that the deposited particle concentration on the plate $c_{\text{spot}} = c_{\text{gas}}ZEt$, in agreement with Equation (12) in the previous section. We should remember that formation of a top hat deposition

profile assumes that all particles have the same electrical mobility. In cases where the aerosol has a wide distribution of electrical mobilities, and if this is known, it should be possible to predict the particle concentration profile on the substrate. The electrical mobility distribution first has to be divided into smaller bins and then for each bin calculate the size of the spot and particle concentration and then add all bins together. This new concentration profile would not be shaped as a top hat, but rather several top hat concentration profiles combined. Note also that this result holds for any axially symmetric shape of the inlet surface, as long as the electric field on the deposition plate is homogeneous. This means that the deposition spot can in extreme cases be smaller than the aerosol inlet diameter. Simulations show that this is actually a possibility, see Figure S3, and the reason for this is the axial force coming from the nonzero electric field in the inlet pipe. This effect is likely also the reason why the simplified analytic model works so well despite assuming an infinitely thin inlet flow.

The results in the last section demonstrate that the deposition of particles is only governed by the deposition flux of particles at the plate, being the constant drift velocity. As long as this velocity is constant and normal to the plate, and the convective field is divergence free, then this model could be extended to other types of particle deposition. In cases where the convective field is not divergence free, this model could still be a valid approximation, provided that the divergence does not affect the deposition significantly. Holunga, Brunelli, and Flagan (2013), demonstrated a tool, similar to the ESP in this work, for homogeneous deposition of nanoparticles using thermophoretic deposition. The particles were, in that case, exposed to a constant thermophoretic velocity, to compare with the constant drift velocity v_d used in this work. By replacing the drift velocity in Equation (11) with the thermophoretic velocity presented in their work, our equation accurate predicts the spot radii reported in their work. We can thus use our simplified expression to calculate the spot radius for this tool, despite that the thermal field is not considered as divergence free. The overall impact on the deposition due to the divergence is in this case small, however, and can therefore be neglected.

Conclusions

To summarize, we have used experiment, simulation and mathematical analysis to determine the exact relation between the deposition spot and the deposition parameters in an ESP. COMSOL Multiphysics has here proven to be a useful way to simulate the macroscopic trajectories of a collection of nanoparticles in a gas flow, combined with an electric field and could most likely be used for other aerosol applications. The analytical models demonstrate why the ESP process is very robust, with uniform particle distribution and well-defined spot size. Based on these results we proposed a simple formula for the deposition spot radius and deposited particle concentration based on only a few key variables. This can be used to predict the particle concentration on the substrate as well as tuning the deposition spot size to the same size as the substrate in order to avoid particle waste and minimize deposition time. Finally, it has not escaped our attention that the mathematical approach used in this article may prove useful in other particle deposition studies, and may also be extended to more complex deposition geometries or deposition mechanisms.

Acknowledgments

The authors wish to thank Robert Hallberg for assistance in data collection and for valuable discussions.

Funding

The experimental part of this work was performed in Lund Nano Lab, part of Myfab research infrastructure. We acknowledge financial support from NanoLund and from the Swedish Research Council (Grant No. 2013-05280).

References

Cheng, Y. S., H. C. Yeh, and G. M. Kanapilly. 1981. Collection efficiencies of a point-to-plane electrostatic precipitator. *Am. Ind. Hygiene Assoc. J.* 42 (8):605–10. doi:10.1080/15298668191420350.

Choi, H., S. Kang, W. Jung, Y-h Jung, S. J. Park, D. S. Kim, and M. Choi. 2015. Controlled electrostatic focusing of charged aerosol nanoparticles via an electrified mask. *J. Aerosol Sci.* 88:90–7. doi:10.1016/j.jaerosci.2015.05.017.

Dixkens, J., and H. Fissan. 1999. Development of an electrostatic precipitator for off-line particle analysis. *Aerosol Sci. Technol.* 30 (5):438–53. doi:10.1080/027868299304480.

Fierz, M., R. Kaegi, and H. Burtscher. 2007. Theoretical and experimental evaluation of a portable electrostatic TEM sampler. *Aerosol Sci. Technol.* 41 (5):520–8. doi:10.1080/02786820701253327.

Hallberg, R. T., L. Ludvigsson, C. Preger, B. O. Meuller, K. A. Dick, and M. E. Messing. 2017. Hydrogen-assisted spark discharge generated metal nanoparticles to prevent oxide formation. *Aerosol Sci. Technol.* 52 (3):347–58. doi:10.1080/02786826.2017.1411580.

Hinds, W. C. 1999. *Aerosol technology: Properties, behavior, and measurement of airborne particles*, 2nd ed. New York: John Wiley & Sons, Inc.

Holunga, D. M., N. A. Brunelli, and R. C. Flagan. 2013. A Tool for Uniform Coating of 300-Mm Wafers with Nanoparticles. *J. Nanopart. Res.* 15 (11):2027. doi:10.1007/s11051-013-2027-1.

John, F. 1982. Partial differential equations. In *Applied mathematical sciences*, 4th ed. Vol. 1. New York, NY: Springer-Verlag.

Kala, S., M. Rouenhoff, R. Theissmann, and F. E. Kruis. 2012. Synthesis and film formation of monodisperse nanoparticles and nanoparticle pairs. In *Nanoparticles from the gasphase: formation, structure, properties*, eds. Axel Lorke, Markus Winterer, Roland Schmechel, and Christof Schulz, 99–119. Berlin, Heidelberg: Springer Berlin Heidelberg. 10.1007/978-3-642-28546-2_4.

Karlsson, M. N. A., K. Deppert, L. S. Karlsson, M. H. Magnusson, J. O. Malm, and N. S. Srinivasan. 2005. Compaction of agglomerates of aerosol nanoparticles: A compilation of experimental data. *J. Nanopart. Res.* 7 (1): 43–9. doi:10.1007/s11051-004-7218-3.

Kim, H., J. Kim, H. Yang, J. Suh, T. Kim, B. Han, S. Kim, D. S. Kim, P. V. Pikhitsa, and M. Choi. 2006. Parallel patterning of nanoparticles via electrodynamic focusing of charged aerosols. *Nature Nanotech.* 1 (2):117–21. doi:10.1038/nnano.2006.94.

Knutson, E. O., and K. T. Whitby. 1975. Aerosol classification by electric mobility: Apparatus, theory, and applications. *J. Aerosol Sci.* 6 (6):443–51. doi:10.1016/0021-8502(75)90060-9.

Krinke, T. J., K. Deppert, M. H. Magnusson, F. Schmidt, and H. Fissan. 2002. Microscopic aspects of the deposition of nanoparticles from the gas phase. *J. Aerosol Sci.* 33 (10):1341–59. doi:10.1016/S0021-8502(02)00074-5.

Krinke, T. J., H. Fissan, K. Deppert, M. H. Magnusson, and L. Samuelson. 2001. Positioning of nanometer-sized particles on flat surfaces by direct deposition from the gas phase. *Appl. Phys. Lett.* 78 (23):3708–10. doi:10.1063/1.1377625.

Liu, B. Y. H., K. T. Whitby, and H. H. S. Yu. 1967. Electrostatic Aerosol Sampler for Light and Electron Microscopy. *Rev. Sci. Instrum.* 38 (1):100–2. doi:10.1063/1.1720491.

Logan, J. D. 1994. *An introduction to nonlinear partial differential equations*, 2nd ed. New York: John Wiley & Sons, Inc.

Magnusson, M. H., B. J. Ohlsson, M. T. Björk, K. A. Dick, M. T. Borgström, K. Deppert, and L. Samuelson. 2014. Semiconductor nanostructures enabled by aerosol technology. *Front. Phys.* 9 (3):398–418. doi:10.1007/s11467-013-0405-x.

McKibbin, S. R., S. Yngman, O. Balmes, B. O. Meuller, S. Tågerud, M. E. Messing, G. Portale, M. Sztucki, K. Deppert, L. Samuelson, et al, 2019. In situ observation of synthesized nanoparticles in ultra-dilute aerosols via X-ray scattering. *Nano Res.* 12 (1):25–31. doi:10.1007/s12274-018-2170-1.

Messing, M. E., K. A. Dick, L. R. Wallenberg, and K. Deppert. 2009. Generation of size-selected gold nanoparticles by spark discharge — for growth of epitaxial nanowires. *Gold Bull.* 42 (1):20–6. doi:10.1007/BF03214902.

Messing, M. E., R. Westerström, B. O. Meuller, S. Blomberg, J. Gustafson, J. N. Andersen, E. Lundgren, R. van Rijn, O. Balmes, H. Bluhm, et al, 2010. Generation of Pd model catalyst nanoparticles by spark discharge. *J. Phys. Chem. C* 114 (20):9257–63. doi:10.1021/jp101390a.

Meuller, B. O., M. E. Messing, D. L. J. Engberg, A. M. Jansson, L. I. M. Johansson, S. M. Norlén, N. Tureson, and K. Deppert. 2012. Review of spark discharge generators for production of nanoparticle aerosols. *Aerosol Sci. Technol.* 46 (11):1256–70. doi:10.1080/02786826.2012.705448.

Ouf, F.-X., P. Parent, C. Laffon, I. Marhaba, D. Ferry, B. Marcillaud, E. Antonsson, S. Benkoula, X.-J. Liu, C. Nicolas, et al. 2016. First in-flight synchrotron X-ray absorption and photoemission study of carbon soot nanoparticles. *Sci. Rep.* 6 (1):1–12. (November):. doi:10.1038/srep36495.

Pavlish, J. H., E. A. Sondreal, M. D. Mann, E. S. Olson, K. C. Galbreath, D. L. Laudal, and S. A. Benson. 2003. Status review of mercury control options for coal-fired power plants. *Fuel Process. Technol.* 82 (2-3):89–165. doi:10.1016/S0378-3820(03)00059-6.

Pfeiffer, T. V., J. Feng, and A. Schmidt-Ott. 2014. New developments in spark production of nanoparticles. *Adv. Powder Technol.* 25 (1):56–70. doi:10.1016/j.apt.2013.12.005.

Preger, C., C. Bulbucan, B. O. Meuller, L. Ludvigsson, A. Kostanyan, M. Muntwiler, K. Deppert, R. Westerström, and M. E. Messing. 2019. Controlled oxidation and self-passivation of bimetallic magnetic FeCr and FeMn aerosol nanoparticles. *J. Phys. Chem. C* 123 (26):16083–90. doi:10.1021/acs.jpcc.9b01678.

Schneider, C. A., W. S. Rasband, and K. W. Eliceiri. 2012. NIH image to imageJ: 25 years of image analysis. *Nat. Methods* 9 (7):671–5. doi:10.1038/nmeth.2089.

Schwyn, S., E. Garwin, and A. Schmidt-Ott. 1988. Aerosol generation by spark discharge. *J. Aerosol Sci.* 19 (5): 639–42. doi:10.1016/0021-8502(88)90215-7.

Wiedensohler, A. 1988. An approximation of the bipolar charge distribution for particles in the submicron size range. *J. Aerosol Sci.* 19 (3):387–9. doi:10.1016/0021-8502(88)90278-9.

You, S., and M. Choi. 2007. Numerical simulation of microscopic motion and deposition of nanoparticles via electrodynamic focusing. *J. Aerosol Sci.* 38 (11):1140–9. doi:10.1016/j.jaerosci.2007.08.002.

Zhuang, Y., Y. Jin Kim, T. Gyu Lee, and P. Biswas. 2000. Experimental and theoretical studies of ultra-fine particle behavior in electrostatic precipitators. *J. Electrostatics* 48 (3-4):245–60. doi:10.1016/S0304-3886(99)00072-8.